Chemical Science

ROYAL SOCIETY OF CHEMISTRY

EDGE ARTICLE

View Article Online
View Journal | View Issue

Cite this: *Chem. Sci.*, 2026, **17**, 1656

All publication charges for this article have been paid for by the Royal Society of Chemistry

Enhanced detection of HBV and HCV using Cas13a-FLAP and FGoAI platforms

Xijuan Gu,†[ac] Tianyi Wang,†[b] Lingwei Wu,[a] Jiayun Guan,[a] Xiaoxia Kang,[a] Wenjun Ming,[a] Yidan Zhu,[a] Qian Xu, *[d] Yuling Qin *[a] and Li Wu *[abe]

Hepatitis viruses continue to pose a major global health burden, underscoring the critical role of early diagnosis in achieving effective disease control. Here, a ratiometric fluorescence biosensor based on Cas13a and fluorescent RNA aptamers was developed for the highly efficient detection of hepatitis viruses. The integrated system consists of three functionally coupled modules: (i) duplex-specific nuclease (DSN)-enabled target recognition and sequence-specific cleavage, (ii) Cas13a-activated collateral degradation, and (iii) fluorescent RNA aptamer-based ratiometric biosensor. The proof-of-concept evaluation established limits of detection of 7.4 copies per μL for the hepatitis B virus (HBV) gene and 2.9 copies per μL for the hepatitis C virus (HCV) gene, respectively. Subsequently, image discrimination was performed using a portable fluorescence imaging device. By innovatively merging classical image processing with AI algorithms, the system achieved significantly enhanced stability and anti-interference capability in image analysis. As a result, the efficiency of this platform was successfully validated through the analysis of clinical samples, achieving a specificity of 100% and a sensitivity of over 96.3%, thereby demonstrating its high diagnostic accuracy. The proposed strategy demonstrates significant potential as a sensitive and highly specific diagnostic platform for hepatitis virus detection.

Received 24th July 2025
Accepted 12th November 2025

DOI: 10.1039/d5sc05526a

rsc.li/chemical-science

Introduction

Viral hepatitis has long been recognized as a global public health challenge due to high transmissibility,[1] diverse transmission routes, wide prevalence, and high morbidity,[2] threatening human health.[3] As two predominant subtypes of hepatitis viruses, HBV and HCV affect approximately 254 million and 50 million individuals globally.[4–6] Early diagnosis plays a critical role in the prevention and control of diseases, facilitating improved clinical outcomes and halting disease progression.

Current diagnostic methods for HBV and HCV primarily involve serological assay and nucleic acid detection.[7] Serological assay based on chemiluminescence or fluorescence strategies may yield false results and poor specificity.[8] As a gold standard, polymerase chain reaction (PCR) is widely utilized for nucleic acid detection in clinical applications.[9,10] However, its limitations in terms of low sensitivity and high dependence on specialized equipment hinders its effectiveness in rapid and simple early detection scenarios.[11] On the other hand, alternative amplification strategies, such as loop-mediated isothermal amplification (LAMP)[12] and recombinase polymerase amplification (RPA),[13] may reduce reliance on complex instrumentation; however, these techniques still face challenges related to primer design[14] and quantitative accuracy.[15]

In recent years, clustered regularly interspaced short palindromic repeat (CRISPR)-based molecular diagnostics have become a pivotal tool in next-generation biosensing due to their rapid detection capabilities, high specificity, and adaptability under simple operational conditions.[16,17] PCR or isothermal amplification has been employed to increase the sensitivity further. Nevertheless, two-step methods are associated with greater complexity and an elevated risk of aerosol generation,[18,19] while one-step methods[20,21] are more prone to non-specific cleavage,[22] thereby prompting research into alternative signal transduction mechanisms. Therefore, advanced strategies are urgently needed to meet the sensitivity requirements of CRISPR-based detection methods.

Recently, research advances have demonstrated that CRISPR-based reporting systems, by incorporating fluorescent RNA aptamers, can effectively achieve nucleic acid detection with high signal-to-noise ratios. Tang *et al.* innovatively utilized an RNA fluorescent aptamer as the reporter system for Cas13a, combined with recombinase-aided amplification (RAA), thereby enabling the detection of single-copy viral targets.[23] Similarly,

[a]*Jiangsu Key Laboratory of Advanced Medical Analysis and Public Health, School of Public Health, Nantong University, Nantong, Jiangsu 226019, P. R. China. E-mail: wuli8686@ntu.edu.cn; ylqin@ntu.edu.cn*

[b]*Affiliated hospital of Nantong University, Nantong University, Nantong, Jiangsu 226019, P. R. China*

[c]*Xinglin College, Nantong University, Qidong, Jiangsu 226236, P. R. China*

[d]*School of Artificial Intelligence and Computer Science, Nantong University, Nantong, Jiangsu 226019, P. R. China. E-mail: aicsxuqian@ntu.edu.cn*

[e]*School of Life Sciences, Nantong University, Nantong, Jiangsu 226019, P. R. China*

† These authors contributed equally to this work.

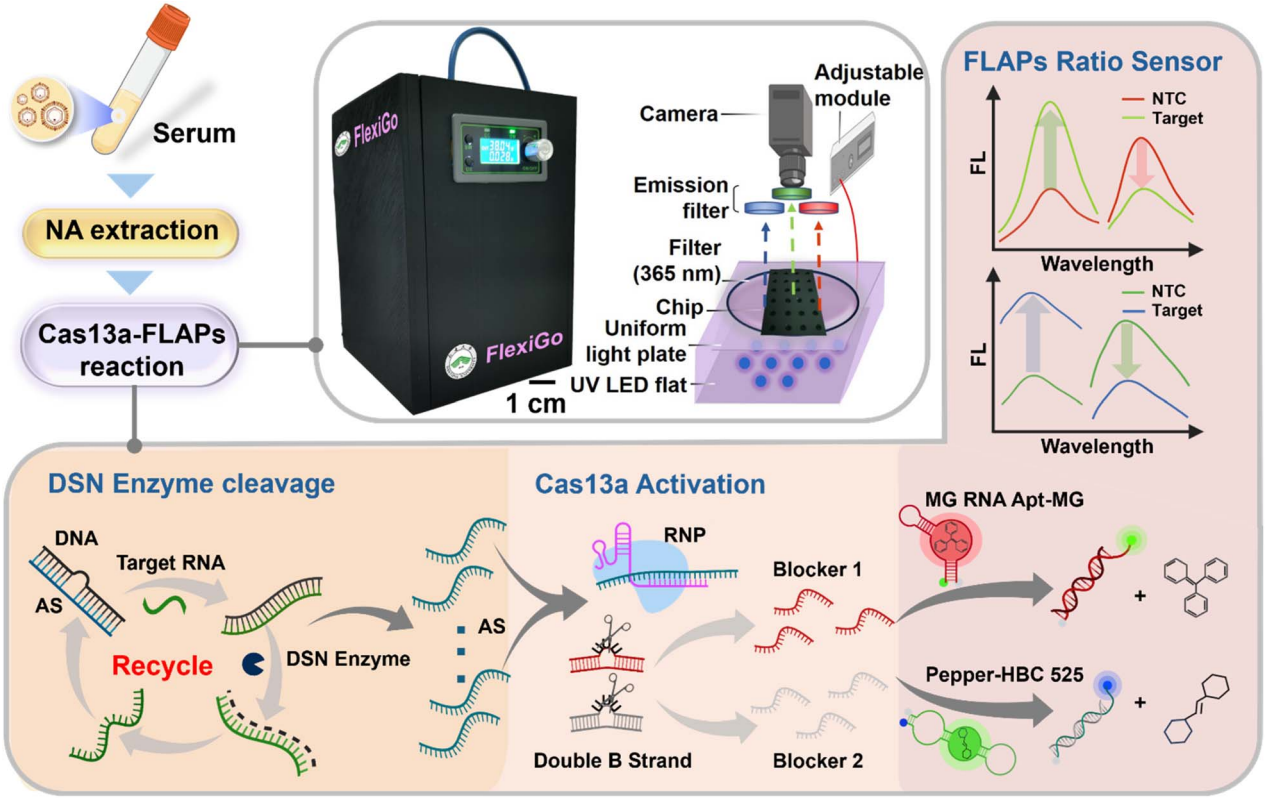

Scheme 1 Illustration of Cas13a-FLAP workflow and operating principles. Convenient FGo workflow: clinical serum samples were collected and then subjected to nucleic acid extraction. The Cas13a-FLAP system consists of three functionally coupled modules: (i) DSN enzyme recognition-cleavage, (ii) Cas13a activation-cleavage, and (iii) fluorescent RNA aptamer-based ratiometric biosensor.

Huo *et al.* developed a label-free fluorescent assay that integrates RPA-Cas12a-DNAzyme with an RNA fluorescent aptamer, achieving ultrasensitive and specific detection of lumpy skin disease virus.[24] Several recent studies have explored the application of CRISPR-Cas systems for detecting HBV and HCV.[25–28] A key commonality among these studies is their reliance on complex nucleic acid amplification technologies (such as LAMP, PCR, or RCA) to pre-amplify viral nucleic acids, followed by CRISPR-Cas system detection typically based on a single fluorescent signal. Despite the excellent performance, these strategies not only complicate primer design but also increase the risk of primer-dimer formation and amplicon contamination, thereby elevating operational complexity and the potential for false-positive results.[29] Furthermore, the single-fluorescence signal readout is susceptible to fluctuations in detection conditions, variations in instrument precision, and interfering substances in samples, thereby compromising both signal stability and quantitative accuracy.[30]

Considering the urgent technical needs for highly efficient detection of HB(C)V, this work proposed a nucleic acid detection strategy based on Cas13a-FLAPs (CRISPR-Cas13a fluorescent light-up aptamers). Specifically, a ratiometric fluorescence sensor based on competitive repressor strands was developed by employing fluorescent RNA aptamers as a secondary signal reporting system. This design enables "signal-switching" detection, thereby facilitating highly sensitive and amplification-free detection of viral nucleic acids (Scheme 1). Primarily, viral nucleic acid was extracted using a silica column lysis method, followed by selective degradation mediated by duplex-specific nuclease (DSN). Subsequently, the Cas13a ribonucleoprotein (RNP) complex undergoes a conformational change upon recognition and binding of the activator strand (AS), enabling specific cleavage of uracil bases within the bubble/blocker strand (double B strand), thereby promoting the release of the blocker strand. The blocker strand, serving as a key signal-converting molecule, specifically hybridizes with the pre-designed fluorescent RNA aptamer, thereby preventing its interaction with the dye. Moreover, a ratiometric fluorescence strategy, based on the individual modification of reporter and quencher groups at the two termini of the RNA aptamer, enables detection with ultra-high sensitivity at the single-copy level. More importantly, the fluorescent signals generated by the Cas13a-FLAP system can be precisely recorded and analyzed using a portable, multifunctional device (FlexiGo, FGo) that is integrated with artificial intelligence (AI) algorithms. This platform provides a valuable reference for developing accurate and robust strategies for the detection of hepatitis viruses and other pathogens.

Results and discussion

Rational design of the DSN enzyme and Cas13a cleavage

The Cas13a-FLAP system is structurally composed of three functional reaction modules: DSN enzyme recognition and cleavage, Cas13a activation and cleavage, and a fluorescent sensor based on FLAPs (Fig. 1a). Initially, the DSN enzyme

triggers the release of the AS strand, thereby activating the Cas13a RNP in module 2. Subsequently, the activated Cas13a complex exerts its *trans*-cleavage activity on the "U" rich regions of the double B strand probe, leading to the release of the blocker strand (BS). Following this, the BS selectively hybridizes with the RNA aptamer through complementary base pairing, enabling ratiometric fluorescence detection. Consequently, each target molecule triggers an exponential amplification of the fluorescence signals, facilitating highly sensitive nucleic acid detection.

Specifically, AS-DNA probes were designed with partial base complementarity and were introduced to establish a DSN enzyme-mediated amplification system. The DNA strands hybridized with the target RNA to form a heteroduplex, which was subsequently cleaved by the DSN enzyme. This process released the target RNA, enabling its repeated participation in the recycling reaction. The system was designed using the FAM fluorophore and BHQ1 quencher to label the AS strand and DNA strand, respectively, where the effective quenching serves as an indicator of successful AS-DNA probe formation (Fig. 1b). Fluorescence recovery was observed upon exposure to the target RNA, suggesting the formation of fully complementary RNA-DNA heteroduplexes. Subsequently, the addition of the DSN enzyme facilitated the cleavage of the DNA strand within the heteroduplex *via* enzymatic digestion, leading to the release of substantial amounts of AS strands. This process promoted the cyclic accumulation of AS strands and enhanced the fluorescent signal. Polyacrylamide gel electrophoresis (PAGE) analysis demonstrated that the AS strand could only be distinguished when the AS-DNA probes, target RNA, and the DSN enzyme were all present concurrently (as illustrated in Fig. S1).

A series of experiments was carried out using varying concentrations of the target molecule to investigate the functional role of the DSN enzyme in the detection of trace target levels. As shown in Fig. S2, the DSN-mediated enzymatic recycling system could induce significant release of the AS strand, even under conditions characterized by low target concentration. A 4-fold increase in fluorescence intensity was observed compared to the group without the DSN enzyme. This DSN enzyme-mediated cycling method can generate a substantial quantity of AS strands, thereby facilitating subsequent detection by the Cas13a module.

In this design, the achievement of efficient ratiometric fluorescence depends on the precise coupling between Cas13a and FLAPs. A series of bubble strands and blocker strands was designed to form double B strands and their variants with varying thermal stabilities. As simulated and calculated using NUPACK (Table S2), the double B strand ($\Delta G_{\text{double B strand}} = -30.94$ kcal mol^{-1}) exhibited a significantly higher binding affinity compared to its three variants ($\Delta G_{\text{Variant 1}} = -19.86$ kcal mol^{-1}, $\Delta G_{\text{Variant 2}} =$

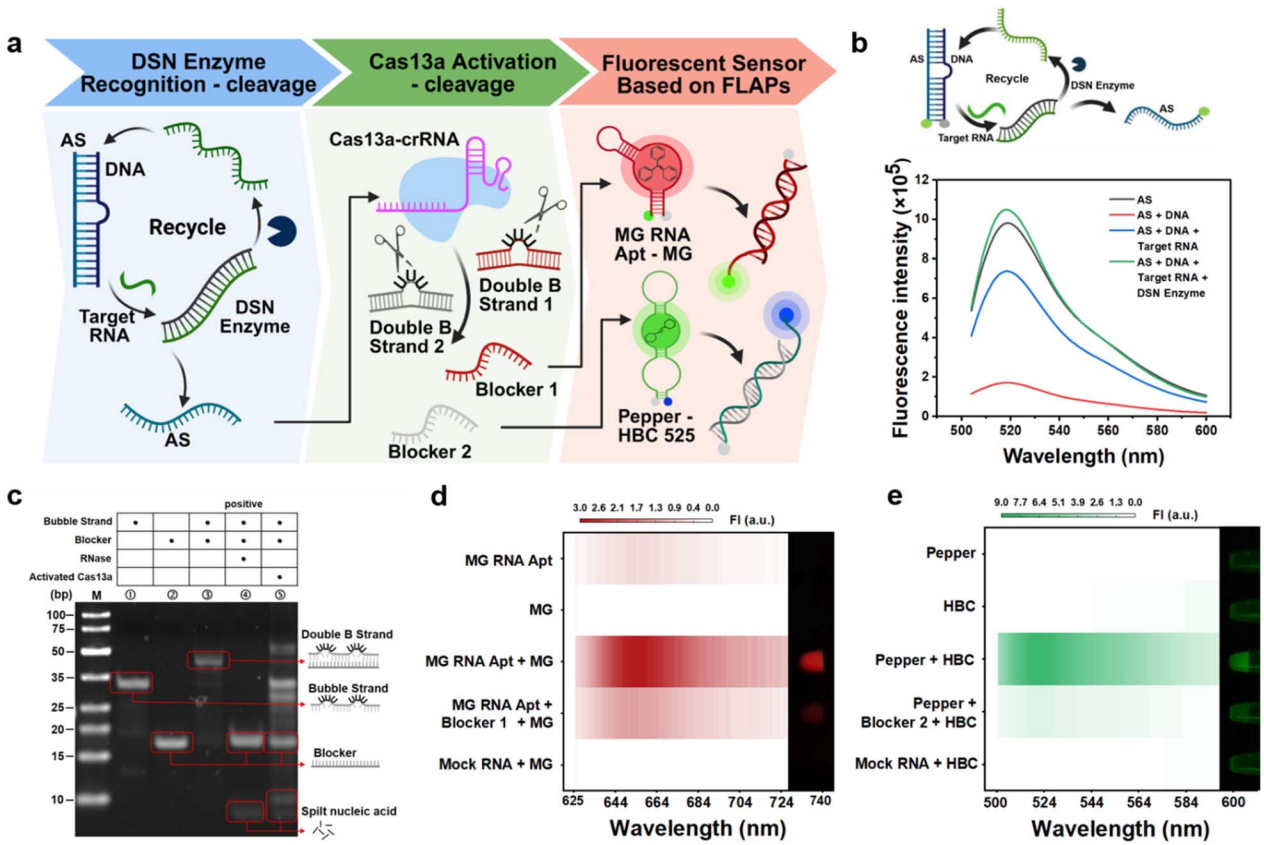

Fig. 1 Feasibility analysis. Schematic representation of (a) the three modules and (b) DSN enzyme recognition-cleavage and corresponding fluorescence spectra. The illustration was created with https://www.biorender.com/. (c) PAGE analysis of the Cas13a *trans*-cleaved double B strand: the bubble strand (lane 1); the blocker strand (lane 2); the bubble strand and blocker strand forming the double B strand (lane 3); the double B strand and RNase (lane 4); the double B strand and activated Cas13a (lane 5). (d) Heatmap and fluorescence imaging for the feasibility analysis of the MG RNA aptamer. (e) Heatmap and fluorescent imaging for the validation of Pepper.

−22.01 kcal mol^{-1}, and $\Delta G_{\text{Variant 3}}$ = −13.31 kcal mol^{-1}, respectively). Subsequently, an RNase assay was conducted to confirm whether the constructed double B strand could undergo *trans*-cleavage by Cas13a. As displayed in Fig. S3, the bubble strand and blocker strand could form a stable double B strand, resulting in reduced migration velocity. Lane 4 demonstrated that RNase was capable of cleaving the U bases on the bubble strand, thereby facilitating the release of the blocker strand. Identically, the results presented in Fig. 1c demonstrated that the double B strand was successfully constructed, implying the feasibility of efficiently coupling the Cas13a and FLAP modules.

Rationally designed FLAPs

A ratiometric fluorescent sensor was constructed by chemically modifying the terminal regions of the RNA aptamer with fluorophores and quenchers. Initial validation of the specificity of RNA aptamer–dye interactions was performed using the unmodified RNA aptamer, a mock RNA sequence and homologous DNA sequences with U-to-T substitutions relative to the RNA aptamer. Two types of RNA aptamers and their corresponding dyes exhibited minimal fluorescence in solution but generated strong fluorescence signals upon target binding (MG: λ_{ex} = 615 nm and λ_{em} = 656 nm; HBC 525: λ_{ex} = 490 nm and λ_{em} = 525 nm) (Fig. S4 and S5). In contrast, no fluorescence signal was detected in the presence of Mock RNA or homologous DNA, thereby confirming the sequence-specific recognition. The potential mechanisms include conformational restriction and electronic modulation. First, the rigid binding pocket of RNA aptamers restricts molecular motion of the dyes, thereby reducing non-radiative energy dissipation and enhancing fluorescence emission. Second, the RNA aptamer may induce steric hindrance or alter the electronic state of the dyes through π–π stacking interactions.[31]

Subsequently, the blocker strands—DNA segments complementary to the RNA aptamers and released by the second module—were introduced into the system. Blocker 1 interfered with the MG-binding loop, thereby inhibiting its interaction with MG and leading to a significant decrease in fluorescence intensity (Fig. 1d). The disruption of blocker 2 led to the breakage of the HBC 525-binding loop, and a similar phenomenon was also observed in the Pepper-HBC 525 system (Fig. 1e). The blocker strand exhibited a preferential binding affinity for the RNA aptamer, thereby effectively disrupting its dye-binding structural conformation (Fig. S6a and b). Based on the above results, the FAM fluorophore (λ_{ex} = 494 nm and λ_{em} = 518 nm) and BHQ1 quencher were conjugated to the terminal ends of the MG RNA aptamer to construct a ratiometric fluorescent sensor. In the absence of blocker 1, the observed fluorescence signal could be attributed to the binding of MG dye to the RNA aptamer, which serves as the negative signal (indicated by the red color). Conversely, in the presence of blocker 1, the fluorescence signal emitted by the aptamer-modified fluorophore shifted toward the green spectrum, indicating a positive signal (Fig. S7a). The terminals of the Pepper aptamer were labelled with the Atto 425 fluorophore (λ_{ex} = 440 nm and λ_{em} = 484 nm) and the BHQ1 quencher. Parallel results were observed upon the introduction of blocker 2 into the Pepper-HBC 525 system (blue-to-green transition, Fig. S7b). Computational modeling using NUPACK confirmed that the hybridization between the RNA aptamer and the blocker exhibited the lowest Gibbs free energy ($\Delta G_{\text{MG RNA aptamer and blocker 1}}$ = −66.02 kcal mol^{-1} and $\Delta G_{\text{Pepper and blocker 2}}$ = −54.16 kcal mol^{-1}). These findings indicated thermodynamically favorable binding interactions, which were consistent with the electrophoretic data.

Characterization of Cas13a-FLAPs

Following the successful validation of the aforementioned submodules, feasibility experiments were performed on the complete Cas13a-FLAP system. PAGE analysis was employed to examine

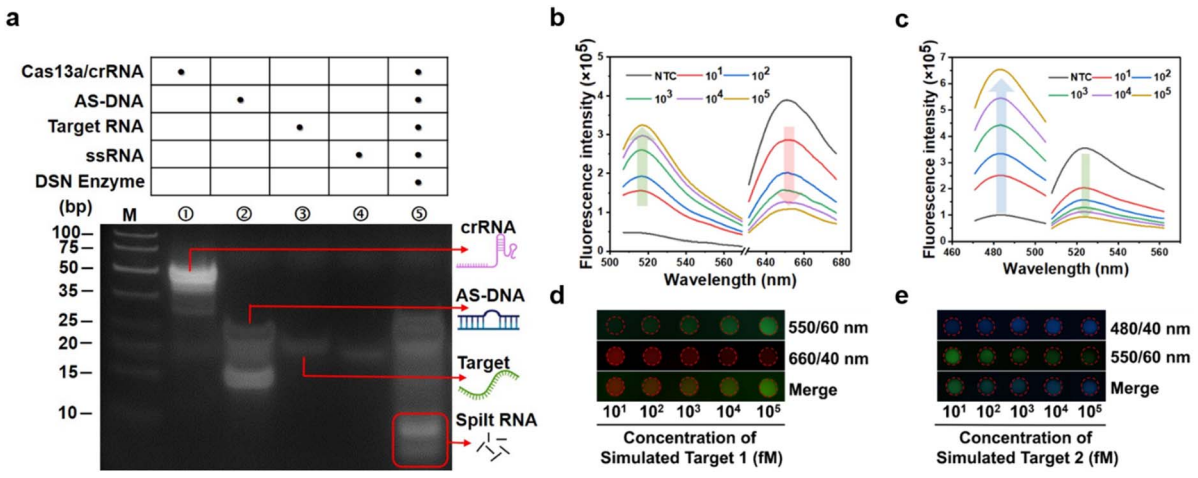

Fig. 2 Validation of the Cas13a-FLAP system. (a) PAGE analysis of the DSN enzyme recycling and Cas13a activation. Lane 1: 500 nM crRNA and 200 nM Cas13a. Lane 2: 250 nM AS-DNA heteroduplex. Lane 3: 250 nM Target RNA. Lane 4: 500 nM single-stranded RNA. Lane 5: all reaction components. (b) Correlation between dual-channel fluorescence signals (FAM and MG) and gradient concentrations of simulated target 1. (c) Correlation between dual-channel fluorescence signals (Atto 425 and HBC 525) and gradient concentrations of simulated target 2. (d) Fluorescence images obtained from the Cas13a-FLAP system at various concentrations of simulated target 1. (e) Fluorescence images demonstrating the Cas13a-FLAP system responses to serial dilutions of simulated target 2.

whether the DSN enzyme can cyclically release AS strands and subsequently activate the Cas13a protein. In Fig. 2a, distinct bands were observed in the low molecular weight range (<10 bp) under conditions where all reaction components were present (lane 5), confirming that the AS strands released by the DSN enzyme effectively activated the *trans*-cleavage ability of Cas13a. Based on the data obtained from module I, low-concentration targets within the range of 10–10^5 fM were selected to rigorously assess the sensitivity of the developed ratiometric fluorescent sensor. The MG RNA aptamer-MG dye system (target 1) demonstrated a concentration-dependent modulation of fluorescence intensity, with a clear inverse correlation between the two signals (Fig. 2b). Moreover, the variation in fluorescence intensity observed in Fig. 2d further confirmed the inverse correlation. Similarly, the Pepper aptamer-HBC 525 dye system (target 2) demonstrated comparable performance characteristics, as shown in Fig. 2c–e. These results provide conclusive evidence supporting the successful development of a Cas13a-FLAP ratiometric biosensor platform.

Optimization of the Cas13a-FLAP assay

To optimize the ratio of double B-strand probes, seven probe variants were constructed for each of the two RNA aptamers, with the ratios of bubble strands to blocker strands set at 1 : 2, 1 : 1.5, 1 : 1, 1.5 : 1, 2 : 1, 2.5 : 1, and 3 : 1. Fluorescence characterization demonstrated that, at the ratio of 2 : 1, bubble strands were capable of fully hybridizing with the blocker strands, thereby minimizing the background signal and improving the signal-to-noise ratio (as shown in Fig. S8a and b).

Subsequently, a series of parameter assays was carried out to determine the optimal experimental conditions. As shown in Fig. S9, the most favourable results were obtained with a probe concentration of 750 nM (Fig. S9a), a DSN enzyme concentration of 4 U μL^{-1} (Fig. S9b), a Cas13a concentration of 5 nM (Fig. S9c), a crRNA concentration of 10 nM (Fig. S9d), a reaction temperature of 37 °C (Fig. S9e), and a reaction time of 20 minutes (Fig. S9f). Additionally, systematic gradient optimization was performed for the concentrations of the MG RNA aptamer (0.3–3 μM), MG dye (50–600 μM), Pepper aptamer (0.3–3 μM), and HBC 525 dye (50–600 μM). As shown in Fig. S10, the optimal performance was achieved at an MG RNA aptamer concentration of 1 μM (Fig. S10a), an MG dye concentration of 450 μM (Fig. S10b), a Pepper aptamer concentration of 2 μM (Fig. S10c), and an HBC dye concentration of 300 μM (Fig. S10d). These results establish a robust experimental basis for the further advancement of sensor technologies.

Evaluation of the Cas13a-FLAP system for hepatitis B and C virus detection

The sensitivity of Cas13a-FLAPs was evaluated by utilizing synthetic RNA transcripts derived from HBV and HCV genomic plasmids. The validation results of the synthesized HBV and HCV genomic plasmids are presented in Fig. S11 and S12. The

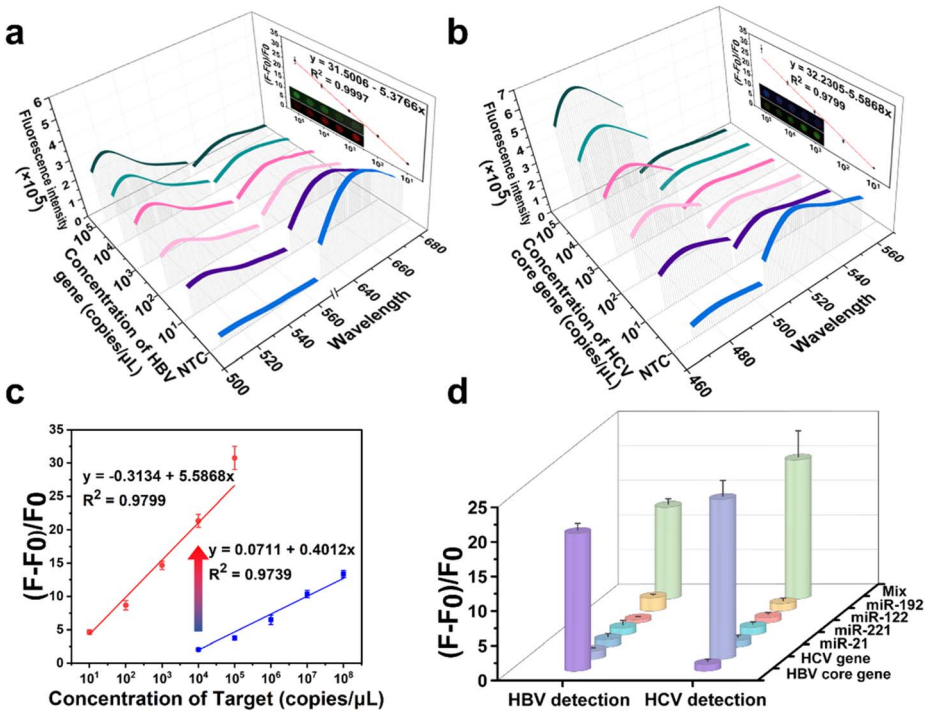

Fig. 3 Assessment of the sensitivity and specificity of the Cas13a-FLAP system for synthesized HBV and HCV genes. Relationship between two fluorescence intensities and various concentrations of the (a) HBV gene (FAM signal and MG signal). (b) HCV gene (Atto425 signal and HBC 525 signal). The inset shows the linear plot of the $(F - F_0)/F_0$ *versus* various gene concentrations and their corresponding fluorescence images. (c) Comparison of calibration curves of the Cas13a-FLAP system (red line) and the traditional amplification-free Cas13a system (blue line) in response to different concentrations of the target. (d) Validation of the cross-reactivity between two hepatitis viruses and several miRNAs associated with hepatocellular carcinoma. The data are shown as mean ± standard deviation ($n = 3$).

single-peak melting curves obtained from qPCR analysis confirmed the specificity of the amplification products.

Additionally, electrophoresis results verified the expected sizes of the HBV (337 bp) and HCV (198 bp) genomic fragments. These findings suggest that the synthesized plasmids exhibit excellent amplification specificity, thereby serving as a reliable template for the subsequent detection of viral nucleic acid.

Based on the optimized parameters, the HBV core gene exhibited exceptional linearity ($y = 31.5006 - 5.3766x$) within the concentration range of 10–10^5 copies per μL ($R^2 = 0.9997$) (Fig. 3a). The proposed Cas13a-FLAP strategy demonstrated remarkable sensitivity, with a limit of detection (LOD) as low as 7.4 copies per μL, representing a substantial improvement over previously reported methods.[32,33] Meanwhile, the Cas13a-FLAP system exhibited a robust linear correlation ($R^2 = 0.9799$) for the HCV gene across the same concentration range (Fig. 3b), with a LOD of 2.9 copies per μL. This represents an improvement in sensitivity of at least three orders of magnitude compared to conventional amplification-free Cas13a-based detection systems (Fig. 3c and S13). The advantage can be attributed to the ratiometric fluorescence strategy, which is based on the ratio of two signals rather than the absolute intensity of a single signal for quantitative analysis.

To further evaluate the specificity of the Cas13a-FLAP strategy, we integrated several microRNAs (miRNAs) that are associated with hepatocellular carcinoma (HCC) into the system (Fig. 3d).[34,35] In the separate detection system, samples containing HBV (or HCV) produced significantly elevated signal ratios, while other miRNAs exhibited minimal responses comparable to background levels, thereby demonstrating the system's excellent resistance to interference and its robust performance. Notably, when HBV (or HCV) was analyzed in combination with HCC-related miRNAs, the system still generated detectable positive signals. The improved detection performance can be attributed to the accurate cleavage and release of the AS strand facilitated by the DSN enzyme, as well as to the highly specific target recognition capability of Cas13a.

Construction of FGo

Current fluorescence detection technologies predominantly rely on large-scale optical instrumentation, which limits their application in point-of-care testing (POCT) environments where miniaturization and rapid response are critical requirements.[36,37] To address this challenge, we have developed a portable fluorescence imaging device, referred to as "FlexiGO" (FGo). The device was designed using modelling software, optimized through an iterative refinement process, and fabricated using 3D printing technology (Fig. S14a). The schematic diagram and device configuration are presented in Fig. 4a. A custom-designed light panel, integrated with a light diffusion plate, was developed to provide uniform illumination across the sample pool. Fluorescence intensity measurements from identical samples in 24 pools were conducted to evaluate the uniformity of the light illumination. As depicted in Fig. 4b and a, uniform illumination was maintained across all detection arrays, as indicated by a relative standard deviation (RSD) of 4.6%. In addition, the background regions of the microarray exhibited minimal non-specific background fluorescence (Fig. S14b), indicating that the constructed device facilitates accurate and efficient simultaneous detection of multiple samples.

For image analysis, we designed and implemented an intelligent, multi-stage processing pipeline to achieve efficient data processing. First, the colour space conversion enables effective multi-channel separation, while an adaptive weighted grayscale algorithm ensures the preservation of key feature information. Next, an enhanced version of the Otsu algorithm is applied to achieve accurate segmentation between the sample and background. Subsequently, connected-component analysis combined with morphological feature parameters allows for the precise identification of target regions. Finally, an adaptive region-growing algorithm integrated with edge-tracking techniques is employed to accurately extract the Regions of Interest (ROI) and identify corresponding detection points (Fig. S15 and Tables S3 and 4). The analytical pipeline innovatively integrates classical image processing techniques with advanced AI algorithms, thereby enhancing the system's practicality, stability, and resistance to interference.

Simulation sample detection

The feasibility of the Cas13a-FLAP and FGoAI (FGo) platform was initially evaluated with 42 synthetic plasmid samples of HBV and HCV (Fig. S17). Among the 42 samples, 15 tested positive for HBV (Fig. 4c), 15 tested positive for HCV (Fig. 4f), and the remaining samples were negative for both viruses. The results presented in Fig. 4d–g demonstrate that the detection outcomes of the as-prepared platform are in agreement with the results obtained using qPCR (Fig. S16). The correlation between Ct values and the $(F - F_0)/F_0$ ratio was illustrated using the Sankey diagrams. As shown in Fig. 4e–h, the Ct values of HBV and HCV exhibited a negative correlation with the $(F - F_0)/F_0$ ratio, suggesting a positive correlation between this ratio and viral load. According to Table S5, the FGo platform demonstrates markedly enhanced performance in viral detection compared to existing methods.

Analysis of clinical samples

We further evaluated the performance of FGo in detecting clinical hepatitis samples (Fig. 5a and S18a), with qPCR (Fig. S19) results serving as the reference standard. The diagnostic performance of the FGo system was evaluated using receiver operating characteristic (ROC) curve analysis. The results presented in Fig. 5b, c and S18b demonstrated that the FGo system possessed an excellent discriminatory capability between positive and negative samples. Specifically, in the detection of HBV, the area under the curve (AUC) was 0.991, demonstrating a sensitivity of 96.3% and a specificity of 100% (Fig. 5d). HCV detection was performed with enhanced precision, yielding an AUC of 1 (Fig. S18c). Statistical analysis revealed significant differences between positive and negative samples for both HBV and HCV ($p < 0.001$) (Fig. 5e and S18d). The occurrence of a false-negative result in the FGo system may

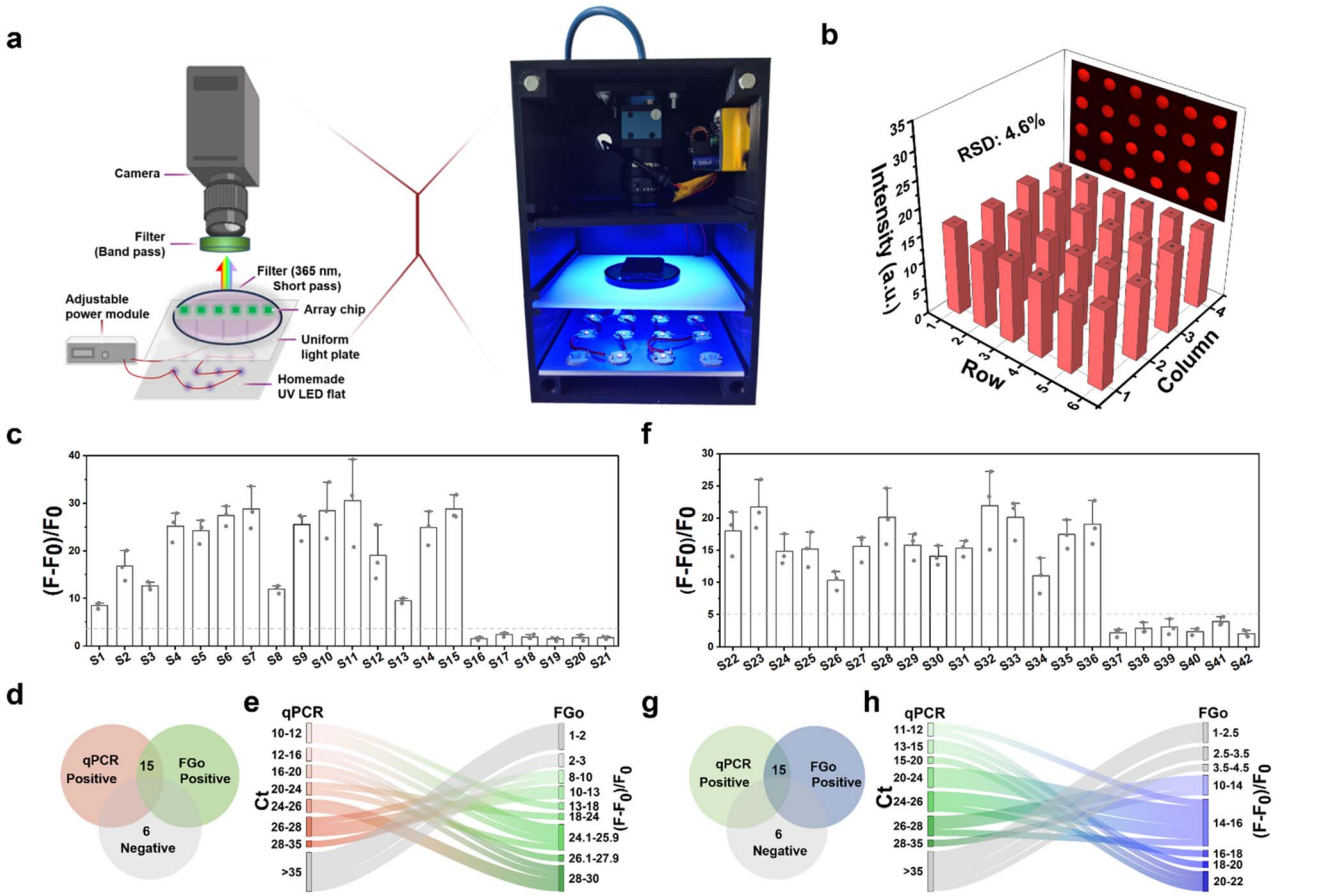

Fig. 4 Design and performance validation of the as-prepared FGo device. (a) Left: the internal structure of a portable nucleic acid detection device. Right: the picture of the in-house developed device. (b) Quantification of fluorescence intensity across all wells in the array chips. Intensity values are expressed as mean ± standard deviation with a relative standard deviation below 4.6%. (c) The ratio results of $(F - F_0)/F_0$ for 21 HBV samples using the FGo platform. (d) Comparison of the performance of qPCR and the FGo assay on the simulation samples of HBV. (e) The Sankey diagram illustrating the correlation between the Ct values and the ratio of $(F - F_0)/F_0$ in HBV detection. (f) The $(F - F_0)/F_0$ values for HCV samples on the FGo platform. (g) Comparison of a classical qPCR method and the FGo platform for detecting HCV (15 positive samples and 6 negative samples). (h) A Sankey diagram illustrating the correlation between Ct values and the $(F - F_0)/F_0$ ratio in HCV detection assays.

be attributed to multiple freeze–thaw cycles following sample collection, which could potentially lead to viral nucleic acid degradation or contamination from undetermined sources.

Experimental

Primer, probes, and synthetic gene plasmid preparation

The primers were designed according to the genotype D M2043 gene of HBV (GenBank accession LT718449.1) and the gene of HCV (GenBank accession AB559564.1) using Primer Premier 5.0 software. All primers, nucleic acid strands, and the synthetic gene plasmid were ordered from Sangon Biotechnology Co., Ltd (Shanghai, China) and are shown in Table S1.

Validation of the Cas13a-FLAP system for target detection

The Cas13a-FLAP system consisted of three reaction modules. The DSN enzyme recognition-cleavage solution comprised AS-DNA probes (10 μM), RNA products at varying concentrations, DSN enzyme (4 U μL^{-1}), reaction buffer [20 mM Tris–HCl (pH 7.4), 100 mM NaCl, 5 mM KCl, 10 mM $MgCl_2$], and DEPC-treated water (up to 20 μL). The reaction mixture was incubated at 37 °C for 20 minutes, followed by heat inactivation of the DSN enzyme at 85 °C for 5 minutes. The Cas13a reaction solution contained Cas13a (5 nM), crRNA (10 nM), TOLOBIO buffer [pH 7.6], double B strands (750 nM), DSN enzyme reaction complex (10 μL), and nuclease-free water (up to 20 μL). Following incubation at 37 °C for 20 minutes, the mixture was heated to 85 °C for 5 minutes to inactivate Cas13a. The FLAP module employed malachite green (MG)[38,39] and (4-((2-hydroxyethyl) (methyl)amino)-benzylidene)-cyanophenyl-acetonitrile (HBC 525)[40,41] as small-molecule dyes. The FLAP reaction system comprised the fluorescent RNA aptamer (MG RNA aptamer at 1 μM or Pepper aptamer at 2 μM), small-molecule dyes (MG dye at 450 μM or HBC 525 at 300 μM), the Cas13a reaction complex, and reaction buffer [40 mM HEPES (pH 7.4), 100 mM KCl, 5 mM $MgCl_2$], with a final volume of 20 μL. The reaction was carried out at room temperature for 7 minutes, followed by fluorescence signal measurement at specific wavelength pairs: FAM (λ_{ex} = 494 nm/λ_{em} = 518 nm), MG (λ_{ex} = 615 nm/λ_{em} = 656 nm), Atto 425 (λ_{ex} = 440 nm/λ_{em} = 484 nm), and HBC 525 (λ_{ex} = 490 nm/λ_{em} = 525 nm).

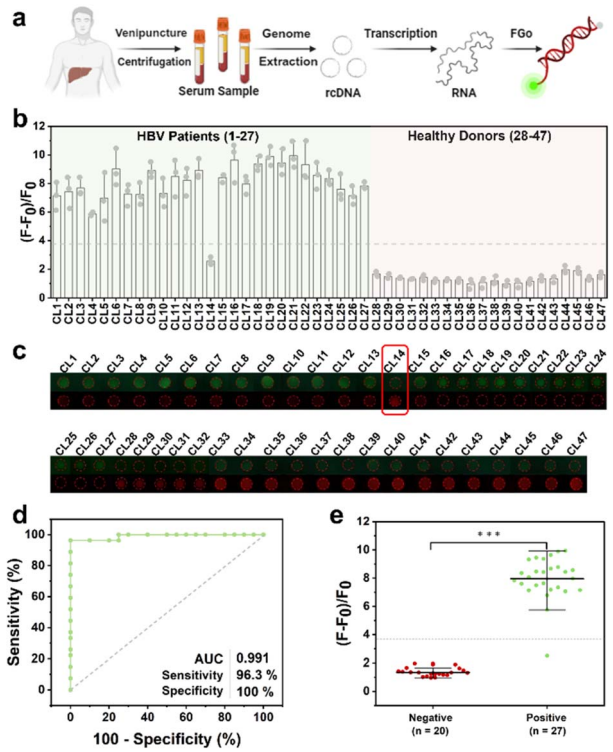

Fig. 5 Clinical application of the FGo platform. (a) Schematic illustration of HBV detection in human plasma samples using the FGo assay. The image was created with https://www.biorender.com/. (b) Estimated $(F - F_0)/F_0$ ratio of HBV in patient plasma samples (samples 1–27) and healthy donor plasma samples (samples 28–47). (c) Fluorescence images of the clinical HBV samples obtained using the FGo platform. (d) ROC curve analysis of the FGo platform. (e) Scatter plot depicting the ratio of $(F - F_0)/F_0$ in 20 negative and 27 positive samples in HBV detection. Statistical significance of the data was assessed by a two-tailed unpaired Student's *t*-test (***$p < 0.001$).

Real-time PCR for HBV and HCV detection

A commercial real-time PCR kit was utilized to detect simulation and clinical samples. Each 20 μL qPCR reaction comprised 10 μL 2× SYBR Master Mix, 200 nM forward and reverse primers, and graded amounts of genomic DNA. Quantitative PCR was performed using a Bio-Rad CFX96 Maestro system. The thermal cycling protocol comprised an initial pre-heating step at 94 °C for 3 minutes, followed by 40 cycles with each cycle consisting of 94 °C for 10 seconds and 60 °C for 30 seconds. Finally, a melting curve analysis was conducted. According to the manufacturer's specifications, samples with cycle threshold (Ct) values ≤35 were interpreted as positive, while those with Ct values >35 were considered negative. The qPCR results for simulated samples are shown in Fig. S16, while clinical sample data are presented in Fig. S19.

Fabrication of the FGo device

The portable fluorescence imaging device was engineered with integrated optical components. It consisted of a home-made UV LED panel, a light modulation element, a light diffusion plate, a set of wavelength-specific filters, a high-throughput microarray chip, and a digital imaging camera (Fig. 4). The three-dimensional (3D) model of the device was designed using SOLIDWORKS software and subsequently manufactured through 3D printing employing polylactic acid (PLA) thermoplastic polymer (Fig. S14a). The UV LED panel comprised twelve serially connected LED beads (3.3 volts per bead), with integrated light-modulation circuitry enabling precise intensity control. This configuration provided a stable irradiance of 20 ± 0.5 W across the 12.5 cm × 13 cm illumination area. The optical detection system was configured with a 365 nm short pass excitation filter, coupled with three bandpass emission filters (480/40 nm, 550/60 nm, and 660/40 nm) to specifically match the emission peak of distinct fluorophores. This multi-channel configuration enables simultaneous detection of multiple fluorescent signals with minimal spectral overlap. The microarray chip was fabricated using polydimethylsiloxane (PDMS) in accordance with the standard fabrication process described in previous research.[42] The experimental images were captured using a miniature CMOS digital camera (5-megapixel resolution) and transmitted *via* a USB 3.0 high-speed interface to a host computer for subsequent image processing and analysis. The system architecture combines these elements into a portable platform suitable for field applications. The image analysis pipeline was implemented entirely using custom Python scripts (Version 3.8.5). We leveraged powerful scientific computing libraries, primarily OpenCV (version 4.5.3.56), Skimage (Version 0.18.3), and Numpy (Version 1.21.2), for all classical image processing steps.

Data analysis

Data were validated through three independent experimental replicates and presented as mean ± standard deviation (SD). Statistical significance was determined by a two-tailed Student's *t*-test and *p*-values below 0.05 were considered statistically significant.

Conclusions

This study presents an ultrasensitive ratiometric fluorescent sensor designed for nucleic acid detection without the need for amplification. By introducing double B strand probes containing U bases, the system enabled precise coupling between Cas13a and FLAPs. Experimental validation demonstrated exceptional performance in detecting hepatitis B and C viruses, with detection limits of 7.4 copies per μL and 2.9 copies per μL, respectively. Additionally, we developed an FGo fluorescence imaging device equipped with a light-modulation optical system, providing uniform illumination and enabling precise detection. The device incorporated an intelligent multi-stage processing pipeline, ensuring high practicality, robustness, and interference resistance. The proposed Cas13a-FLAP and FGo platform exhibited excellent sensitivity and specificity in the detection of clinical HBV and HCV samples in separate reaction systems.

Future research should focus on simultaneously advancing both technical refinement and the expansion of practical applications. Expanding sample diversity and developing more sophisticated deep learning algorithms can enhance detection accuracy and robustness in technical advancement. The platform

shows significant potential for extending into immunology, biochemistry, and molecular diagnostics. This is particularly relevant for infectious disease and point-of-care testing in clinical settings. These developments will collectively enhance public health surveillance capabilities and early-warning systems, leading to more precise disease prevention and control measures.

Ethics approval and consent to participate

All experiments involving human participants were conducted in accordance with the principles of the Declaration of Helsinki. The study protocol was approved by the Ethics Committee of Nantong University (TDLS: 2025-01). Informed consent was obtained from the human participants of this study.

Author contributions

Xijuan Gu: conceptualization, methodology, investigation, and writing – review & editing; Tianyi Wang: sample acquisition and nucleic acid extraction; Lingwei Wu: scientific experiment; Jiayun Guan: conceptualization and methodology; Xiaoxia Kang: 3D printed device design; Wenjun Ming: scientific experiment; Yidan zhu: 3D printed device printing; Qian Xu: data curation and formal analysis; Li Wu: conceptualization and funding acquisition; Yuling Qin: supervision, writing – reviewing and editing, project administration, and funding acquisition.

Conflicts of interest

There are no conflicts to declare.

Data availability

The data that support the findings of this study are available on request from the corresponding author.

Supplementary information (SI): reagents and materials, preparation of probes, gel electrophoresis, *in vitro* transcription, clinical samples, and calculation of the limit of detection (LOD); PAGE analysis of the DSN enzyme recognition-cleavage module, validation of the DSN enzyme in trace target detection, PAGE analysis of RNase cleaving double B strand, heatmap, fluorescent imaging, and fluorescence intensity for the validation of MG RNA aptamer and MG dye, heatmap, fluorescent imaging, and fluorescence intensity for the validation of Pepper aptamer and HBC 525 dye, PAGE analysis of the RNA aptamers and blockers, validation of a ratiometric fluorescent sensor, optimization of the ratio between the bubble strand and the blocker, optimization of the DSN enzyme and Cas13a module, comparison of the Cas13a-FLAPs system with the traditional Cas13a reaction, the structure and image of the device, intelligent Image Analysis Pipeline, qPCR of simulation sample detection, fluorescence images of the simulation samples using the FGo device, clinical application of HCV using the FGo platform, and qPCR of HBV and HCV detection (Fig. S1–S19); and nucleic acid sequences used in this study, the establishment of double B strand sequences, artificial intelligence models, and the comparison between FGo and other virus detection methods (Tables S1–S5). See DOI: **https://doi.org/10.1039/d5sc05526a**.

Acknowledgements

This work was supported by the National Natural Science Foundation of China (82373456 and 32171452), the National Key R&D Program of China (Grant No. 2024YFA1613800), the Excellent Youth Foundation of Jiangsu Scientific Committee (BK20220060), the Jiangsu Innovative and Entrepreneurial Research Team Program (JSSCTD202348), the Research Projects of Nantong Municipal Science and Technology Bureau: Nantong Social Science and Technology Program for People's Livelihood (MS2024023), the Postgraduate Research & Practice Innovation Program of Jiangsu Province (SJCX24_2025), and the Large Instruments Open Foundation of Nantong University.

References

1 C. Thomadakis, I. Gountas, E. Duffell, K. Gountas, B. Bluemel, T. Seyler, F. M. Pericoli, I. Kászoni-Rückerl, Z. El-Khatib, M. Busch, I. Schmutterer, T. Vanwolleghem, S. Klamer, E. Plettinckx, L. Mortgat, D. Van Beckhoven, T. Varleva, M. L. K. Licina, T. N. Blazic, D. Nonkovic, F. Theophanous, V. Nemecek, M. Maly, P. B. Christensen, S. Cowan, K. Rüütel, H. Brummer-Korvenkontio, C. Brouard, G. Steffen, A. Krings, S. Dudareva, R. Zimmermann, G. Nikolopoulou, Z. Molnár, E. Kozma, M. Gottfredsson, N. Murphy, L. A. Kondili, M. E. Tosti, A. R. Ciccaglione, B. Suligoi, R. Nikiforova, R. Putnina, L. Jancoriene, C. Seguin-Devaux, T. Melillo, A. Boyd, M. van der Valk, E. O. de Coul, R. Whittaker, H. Klovstad, M. Stepien, M. Rosinska, C. Valente, R. T. Marinho, O. Popovici, M. Avdicová, J. Kerlik, I. Klavs, M. Maticic, A. Diaz, J. del Amo, J. L. Ederth, M. Axelsson and G. Nikolopoulos, *Lancet Reg. Health-Eu.*, 2024, **36**, 100792.
2 F. Cui, S. Blach, C. Manzengo Mingiedi, M. A. Gonzalez, A. Sabry Alaama, A. Mozalevskis, N. Séguy, B. B. Rewari, P. L. Chan, L. V. Le, M. Doherty, N. Luhmann, P. Easterbrook, M. Dirac, C. de Martel, S. Nayagam, T. B. Hallett, P. Vickerman, H. Razavi, O. Lesi and D. Low-Beer, *Lancet Gastroenterol.*, 2023, **8**, 332–342.
3 D. L. Thomas, *N. Engl. J. Med.*, 2019, **380**, 2041–2050.
4 J. An, D. A. Park, M. J. Ko, S. B. Ahn, J. J. Yoo, D. W. Jun and S. Y. Yim, *J. Pers. Med.*, 2022, **12**, 1517.
5 K. N. Ly, S. Yin and P. R. Spradling, *JAMA Netw. Open*, 2022, **5**, e2219170.
6 A. L. Migdal, R. Jagannathan, E. Qayed, K. Cusi, R. G. McCoy, F. J. Pasquel and L. S. Miller, *JAMA Netw. Open*, 2022, **5**, e2142282.
7 X. Ye, W. Xiong, X. Xu, J. Zeng, H. Xie, B. Li, B. He, L. Chen and Q. Mo, *BMC Infect. Dis.*, 2024, **24**, 909.
8 V. Soriano, A. Aguilera, R. Benito, R. González-Díez, E. Miró, P. Liendo, J. C. Rodríguez-Diaz, T. Cabezas, A. Richart, J. M. Ramos, L. Barea, C. Álvarez, A. Treviño, F. Gómez-

Gallego, O. Corral and C. de Mendoza, *Liver Int.*, 2023, **43**, 1015–1020.
9 M. Gaňová, H. Zhang, H. Zhu, M. Korabečná and P. Neužil, *Biosens. Bioelectron.*, 2021, **181**, 113155.
10 X. Dong, Y. Huang and D. Jiang, *Anal. Chem.*, 2022, **94**, 10304–10307.
11 E. Valera, A. Jankelow, J. Lim, V. Kindratenko, A. Ganguli, K. White, J. Kumar and R. Bashir, *ACS Nano*, 2021, **15**, 7899–7906.
12 A. Ganguli, A. Mostafa, J. Berger, J. Lim, E. Araud, J. Baek, S. A. Stewart de Ramirez, A. Baltaji, K. Roth, M. Aamir, S. Aedma, M. Mady, P. Mahajan, S. Sathe, M. Johnson, K. White, J. Kumar, E. Valera and R. Bashir, *Anal. Chem.*, 2021, **93**, 7797–7807.
13 J. Lim, S. Zhou, J. Baek, A. Y. Kim, E. Valera, J. Sweedler and R. Bashir, *Small*, 2024, **20**, e2307959.
14 W. Zeng, W. Chen, Y. Liu, T. Zhang, C. Zhai, W. Li, L. Wang, C. Zhang, Q. Zeng, F. Wang and L. Ma, *Biosens. Bioelectron.*, 2024, **259**, 116400.
15 F. Deng, Y. Li, B. Yang, R. Sang, W. Deng, M. Kansara, F. Lin, S. Thavaneswaran, D. M. Thomas and E. M. Goldys, *Nat. Commun.*, 2024, **15**, 1818.
16 J. S. Gootenberg, O. O. Abudayyeh, J. W. Lee, P. Essletzbichler, A. J. Dy, J. Joung, V. Verdine, N. Donghia, N. M. Daringer, C. A. Freije, C. Myhrvold, R. P. Bhattacharyya, J. Livny, A. Regev, E. V. Koonin, D. T. Hung, P. C. Sabeti, J. J. Collins and F. Zhang, *Science*, 2017, **356**, 438.
17 X. Gu, Q. Tang, Y. Zhu, C. Sun, L. Wu, H. Ji, Q. Wang, L. Wu and Y. Qin, *Biosens. Bioelectron.*, 2024, **261**, 116449.
18 Z. Zhao, R. Wang, X. Yang, J. Jia, Q. Zhang, S. Ye, S. Man and L. Ma, *ACS Nano*, 2024, **18**, 33505–33519.
19 J. P. Broughton, X. Deng, G. Yu, C. L. Fasching, V. Servellita, J. Singh, X. Miao, J. A. Streithorst, A. Granados, A. Sotomayor-Gonzalez, K. Zorn, A. Gopez, E. Hsu, W. Gu, S. Miller, C. Y. Pan, H. Guevara, D. A. Wadford, J. S. Chen and C. Y. Chiu, *Nat. Biotechnol.*, 2020, **38**, 870–874.
20 Z.-H. Cheng, X.-Y. Luo, S.-S. Yu, D. Min, S.-X. Zhang, X.-F. Li, J.-J. Chen, D.-F. Liu and H.-Q. Yu, *Nat. Commun.*, 2025, **16**, 1166.
21 X. Tong, K. Zhang, Y. Han, T. Li, M. Duan, R. Ji, X. Wang, X. Zhou, Y. Zhang and H. Yin, *Nat. Chem. Biol.*, 2024, **20**, 885–893.
22 C. Hui, F. Ying, L. Feng, T. Chunyan, X. Naihan, J. Yuyang and T. Ying, *Biosens. Bioelectron.*, 2023, **247**, 115929.
23 X. Wang, X. Deng, Y. Zhang, W. Dong, Q. Rao, Q. Huang, F. Tang, R. Shen, H. Xu, Z. Jin, Y. Tang and D. Du, *Biosens. Bioelectron.*, 2024, **257**, 116268.
24 G. Cao, N. Yang, J. Yang, J. Li, L. Wang, F. Nie, D. Huo and C. Hou, *Anal. Chem.*, 2024, **96**, 10927–10934.
25 S. N. Shahni, S. Albogami, I. Azmi, B. Pattnaik, R. Chaudhuri, K. Dev, J. Iqbal, A. Sharma and T. Ahmad, *J. Nucleic Acids*, 2024, **2024**, 8819834.
26 R. Ding, J. Long, M. Yuan, X. Zheng, Y. Shen, Y. Jin, H. Yang, H. Li, S. Chen and G. Duan, *Int. J. Mol. Sci.*, 2021, **22**, 4842.
27 N. Kham-Kjing, N. Ngo-Giang-Huong, K. Tragoolpua, W. Khamduang and S. Hongjaisee, *Diagnostics*, 2022, **12**, 1524.
28 X. Zhang, Y. Tian, L. Xu, Z. Fan, Y. Cao, Y. Ma, H. Li and F. Ren, *Hepatol. Int.*, 2022, **16**, 306–315.
29 H. J. Li, J. Yang, G. F. Wu, Z. Y. Weng, Y. Song, Y. X. Zhang, J. A. Vanegas, L. Avery, Z. Gao, H. Sun, Y. P. Chen, K. D. Dieckhaus, X. Gao and Y. Zhang, *Angew. Chem. Int. Edit*, 2022, **61**, e202203826.
30 Q. Feng, T. Wu, H. Wang, M. Wu, B. Dou and P. Wang, *Chem. Commun.*, 2024, **60**, 2046–2049.
31 X. Chen, D. Zhang, N. Su, B. Bao, X. Xie, F. Zuo, L. Yang, H. Wang, L. Jiang, Q. Lin, M. Fang, N. Li, X. Hua, Z. Chen, C. Bao, J. Xu, W. Du, L. Zhang, Y. Zhao, L. Zhu, J. Loscalzo and Y. Yang, *Nat. Biotechnol.*, 2019, **37**, 1287–1293.
32 K. Shi, S. Y. Xie, R. Y. Tian, S. Wang, Q. Lu, D. H. Gao, C. Y. Lei, H. Z. Zhu and Z. Nie, *Sci. Adv.*, 2021, **7**, eabc7802.
33 R. Lai, M. Lai, B. He, B. Li, L. Huang, H. Xie and L. Chen, *Microchim. Acta*, 2025, **192**, 422.
34 L. Kang, J. Wu, X. Lin, J. Li, N. Duan, Z. Wang and S. Wu, *Biosens. Bioelectron.*, 2024, **264**, 116628.
35 R. Li, Y. Chen, R. Pan, S. Hu, S. Zhao, J. Tian and J. Zhao, *Anal. Chem.*, 2024, **96**, 18096–18103.
36 X. Gu, A. Pan, L. Wu, J. Zhang, Z. Xu, T. Wen, M. Wang, X. Shi, L. Wu and Y. Qin, *Chem. Sci.*, 2024, **15**, 18411–18418.
37 M. Lin, Z. Qiu, M. Hao, W. Qi, T. Zhang, Y. Shen, H. Xiao, C. Liang, L. Xie, Y. Jiang, M. Cheng, T. Tian and X. Zhou, *Nat. Commun.*, 2025, **16**, 5597.
38 C. H. Woo, S. Jang, G. Shin, G. Y. Jung and J. W. Lee, *Nat. Biomed. Eng.*, 2020, **4**, 1168–1179.
39 Y. Park, J. Yoon, J. Lee, S. Lee and H. G. Park, *Biosens. Bioelectron.*, 2022, **204**, 114071.
40 T. Endoh, J. H. Tan, S. B. Chen and N. Sugimoto, *Anal. Chem.*, 2023, **95**, 976–985.
41 R. Zheng, R. Wu, Y. Liu, Z. Sun, Z. Xue, Y. Bagheri, S. Khajouei, L. Mi, Q. Tian, R. Pho, Q. Liu, S. Siddiqui, K. Ren and M. You, *Nucleic Acids Res.*, 2024, **52**, e67.
42 Y. Qin, J. E. Kreutz, T. Schneider, G. S. Yen, E. S. Shah, L. Wu and D. T. Chiu, *Lab Chip*, 2022, **22**, 4729–4734.